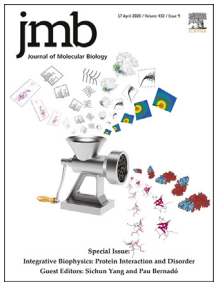

The Pierced Lasso Topology Leptin has a Bolt on Dynamic Domain Composed by the Disordered Loops I and III

Jens Danielsson[1], Jeffrey Kenneth Noel[2], Jennifer Michelle Simien[3], Brendan Michael Duggan[4], Mikael Oliveberg[1], José Nelson Onuchic[5,6], Patricia Ann Jennings[7] and Ellinor Haglund[3]

*1 - **Department of Biochemistry and Biophysics,** Stockholm University, Stockholm, Sweden*
*2 - **Kristallographie Max Delbrück Center for Molecular Medicine,** Berlin, Germany*
*3 - **The Department of Chemistry,** University of Hawaii, Manoa, Honolulu, USA*
*4 - **Skaggs School of Pharmacy and Pharmaceutical Sciences,** University of California at San Diego, La Jolla, USA*
*5 - **Center for Theoretical Biological Physics,** Rice University, Houston, USA*
*6 - **Department of Physics and Astronomy,** Department of Chemistry, And Department of Biosciences, Rice University, Houston, USA*
*7 - **Department of Chemistry and Biochemistry,** The University of California at San Diego, La Jolla, USA*

***Correspondence to Ellinor Haglund** and **Jens Danielsson**: ellinorh@hawaii.edu, jens.danielsson@dbb.su.se*
https://doi.org/10.1016/j.jmb.2020.01.035
Edited by Sichun Yang

Abstract

Leptin is an important signaling hormone, mostly known for its role in energy expenditure and satiety. Furthermore, leptin plays a major role in other proteinopathies, such as cancer, marked hyperphagia, impaired immune function, and inflammation. In spite of its biological relevance in human health, there are no NMR resonance assignments of the human protein available, obscuring high-resolution characterization of the soluble protein and/or its conformational dynamics, suggested as being important for receptor interaction and biological activity. Here, we report the nearly complete backbone resonance assignments of human leptin. Chemical shift-based secondary structure prediction confirms that in solution leptin forms a four-helix bundle including a pierced lasso topology. The conformational dynamics, determined on several timescales, show that leptin is monomeric, has a rigid four-helix scaffold, and a dynamic domain, including a transiently formed helix. The dynamic domain is anchored to the helical scaffold by a secondary hydrophobic core, pinning down the long loops of leptin to the protein body, inducing motional restriction without a well-defined secondary or tertiary hydrogen bond stabilized structure. This dynamic region is well suited for and may be involved in functional allosteric dynamics upon receptor binding.

Introduction

Energy uptake, storage, and expenditure in an organism must be under tight control to assure energy between meals, as well as avoiding excess uptake and storage, resulting in obesity with its accompanying sequelae [1]. In mammals, the pleiotropic hormone leptin has been shown to have an essential role in regulating energy balance by reducing hunger and increasing energy consumption [2]. Leptin is mainly produced in and excreted by white adipose tissue, the placenta and the gastric epithelium, where gastric leptin seems to be released upon food intake, while adipose and placental leptin are released in proportion to the respective tissue mass [3].

Upon release, leptin circulates in the blood and exerts its function via specific binding to the leptin receptor (LEP-R) [4,5]. LEP-R is a membrane-associated receptor predominantly found in the hypothalamus, although it is also present in lower abundances in several other tissue types [6]. In order to reach its primary target receptor, leptin has to pass the blood-brain barrier. This is facilitated via a saturable transport system that is suggested to involve a carrier protein, a soluble form of LEP-R [7], derived from cleavage of the extracellular part of the receptor [8]. An alternative proposed pathway for leptin to cross

from the blood to the hypothalamus via the cerebrospinal fluid (CSF), is through specialized hypothalamic glial cells called tanycytes. These special ependymal cells are located in the ventricular system and form a barrier between the blood and the CSF [9–11].

Leptin initially binds to LEP-R in a one-to-one stoichiometry, followed by a secondary interaction with an adjacent receptor, inducing a homo-dimerization of the receptor forming a quaternary complex [12–15]. Consequently, leptin has two binding sites to its receptor, putatively (but not necessarily) allosterically coupled where initial binding invokes affinity to the second binding site. Three regions on leptin have been shown to be involved in binding to LEP-R, and are denoted binding sites I, II and III (Fig. 1) [12–16], where binding site II and III seems to be most crucial for recognition and binding. Thus, leptin has to form several essential specific interactions in order to travel from the excreting cells to the target cells and exert its function.

A number of single point mutations in the leptin coding gene are associated with a disease, causing leptin deficiency, which, in turn, results in early-age obesity and hyperphagia [2,17–32]. In silico and experimental characterization of the molecular effects of these mutations show that they can cause leptin deficiency in multiple ways, e.g., through interference with receptor binding or detrimental destabilization, rendering a folding-incompetent protein [33].

Leptin is a relatively small 16 kDa four-helix bundle protein, classified to be part of the long-chain helical cytokine family [34]. However, the structural topology of leptin stands out, as an intramolecular disulfide bond (C96–C146) creates a covalent loop along the primary chain (Fig. 1). In the crystal structure, a section of the polypeptide chain is threaded through this covalent loop generating a "knot-like" topology, or a pierced lasso topology (PLT) [35–40]. Interestingly, a PLT is not unique to leptin, and presently, over 300 PLT proteins have been discovered in the Protein Data Bank [39,40]. The disulfide bond creating the PLT has a significant effect on the stability of leptin, since a reduction of the disulfide bond reduces the stability from 3.4 to 1.8 kcal/mol [35], corresponding to an increase in the unfolded population from 0.3 to 4.6%. Thus, the PLT seems crucial for leptin, as it is already unstable relative to other four-helix bundle proteins [41–45]. In addition to a direct effect on protein stability, we have shown that the PLT is important for leptin receptor interaction and signaling, due to dynamic coupling between the disulfide bond and residues involved in receptor binding [35,38]. Simulation studies found that the reduction of the intramolecular disulfide bond alters the dynamics in the receptor-binding region. Such long-range communication is a common feature of protein dynamics [46–49].

Leptin is, therefore, an example of a system with allosteric long-range dynamic couplings, where the altered dynamics lead to changes in protein function, and thus, make experimental structural-dynamical characterization of leptin of importance. In order to understand leptin function in molecular detail (and mutation-induced malfunction) in molecular detail, we aimed to benchmark the dynamic properties of the free monomeric leptin. Here, we focus on nuclear magnetic resonance (NMR), as it is exceptionally suitable for detailed structural and dynamical studies of proteins in solution [50]. The results show that leptin, in solution, is a well-defined globular monomer but with long loops contributing to an overall dynamic protein. We show that the short, tilted helix 4' in the crystal structure, is only transiently present in solution. Although only transiently present in the free form, it is possibly linked to the function of the bound state. This initial characterization now puts us in a position to investigate, in great detail, e.g., receptor binding, carrier protein binding, and dynamical effects from disease-related mutations.

Results and Discussion

Leptin W100E shows reduced but not abolished transient self-interaction

The wild-type native leptin has previously been shown to transiently form oligomeric species that are prone to precipitate into larger aggregates [51]. Furthermore, the wild-type protein does not form observable crystals putatively due to a heterogeneous native state, large amplitude dynamics, and/or oligomerization [34]. A single point mutation (W100E) reduces self-interaction, resulting in a monomeric species in the crystalline form [34] while preserving function. However, preliminary NMR data suggests that this variant is also involved in transient self-interactions (Supporting Information). To further reduce such transient oligomerization that would efficiently mask the dynamical properties of the monomer, we introduced a second point mutation (W138E), resulting in a tryptophan free protein. Now, NMR data show that this variant is less prone to form oligomers, and the overall structure and spectral properties seem to be unaffected by the second mutation (Supporting Information, Fig. S1), yielding largely overlapping HSQC spectra. This more monomeric tryptophan free form of leptin, leptin^{0Trp}, is used for this study.

Assignment of the backbone resonances

The ^{15}N-(^{1}H)-TROSY spectrum of leptin^{0Trp} shows well-dispersed cross-peaks in the region 7.5–9.6 ppm, archetypical for a folded globular protein of a small to moderate size [50] (Fig. 1). In general, the line widths are uniform and relatively narrow, in line with a monomeric ~16 kDa protein

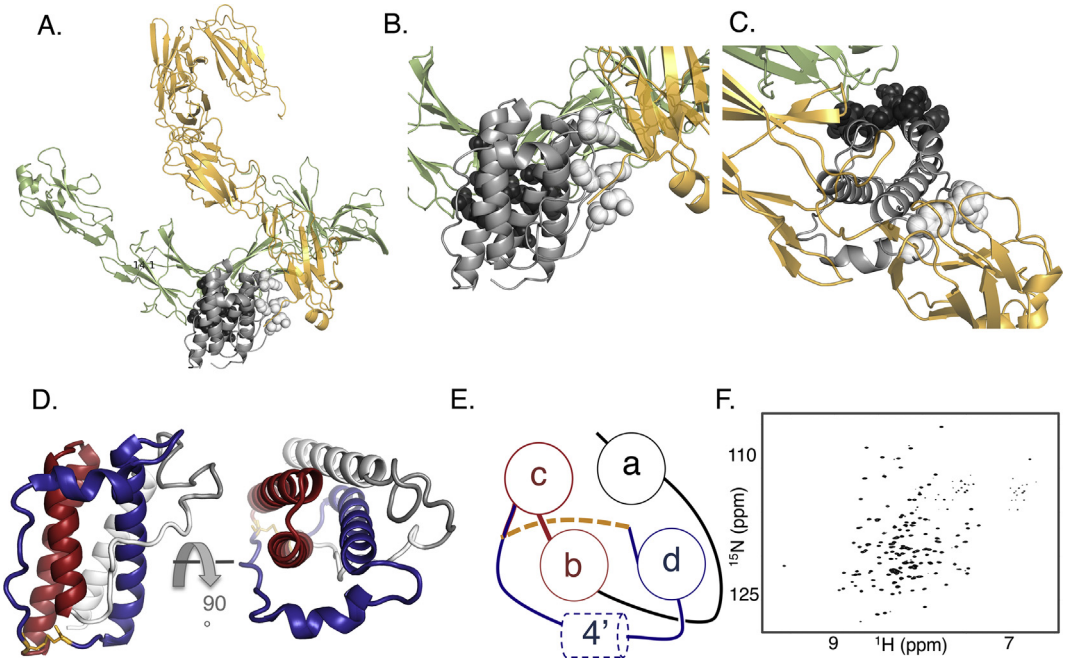

Fig. 1. (A–C) A cartoon representation of leptin binding to the leptin receptor complex. The binding site II (dark grey spheres) and III (white spheres) link together two leptin binding domains (green and orange) of the leptin receptor. Domains 4 and 5 of the receptor interacts with binding site II in leptin to form the initial complex. Once this 1:1 complex is formed, it can maturate into the active complex through linking domain 3 of the receptor to binding site III in leptin [13,14]. (D) Crystal structure representation of leptin (PDB id: 1AX8 [34]), highlighting the pierced lasso topology. Loop I (white) and helix b (red) protrudes the pierced lasso loop, which is formed by loop III and helix d (blue). The light grey part of loop I is modeled from molecular dynamic simulations, as the crystal structure lacks this region. (E) Shows a top view cartoon of the protein with the nomenclature of the four core helices and the bolt-on helix 4', as well as the knot topology. (D) The TROSY spectrum shows well-dispersed, narrow linewidth cross peaks, indicating a folded monomeric species, well suited for NMR analysis.

[52–55]. An obvious requirement for high-resolution NMR studies of leptin^{0Trp} in solution is full or near-full chemical shift assignments. Here, we used a standard set of triple resonance experiments to obtain backbone resonance assignments. In order to increase spectral resolution, we used TROSY-based [56] experiments, and to reduce the experimental time, we used band-selective excitation short transient [57,58] experiments. Using this standard strategy, we obtained 98% assignment of the nonproline amide proton and nitrogen chemical shifts, 94% of the carbonyl shifts, 88% of the C^{α} shifts, and 91% of the nonglycine C^{β} shifts (Supporting Information Table S1). The missing assignments are typically due to signal overlap, ambiguities and/or weak signal intensity. We limited the assignment to the backbone, as a full structural analysis, including the side chains, is beyond the scope of this study, and a high-resolution crystal structure is already solved and published (PDB id: 1AX8 [34]). Nonetheless, the chemical shifts carry indirect information of the structure and can be used to determine whether the crystal structure indeed represents the solution structure.

Secondary structure prediction from chemical shifts

The measured chemical shift values can be compared to the statistical expectation value for a particular nucleus in a particular amino acid in a helical, sheet, or random coil structural state. The expectation values then constitute the defining values of a ruler, with a fully adopted helix or sheet in the ends and random coil somewhere in between. From these values, we can estimate both the nature of the secondary structure, as well as the population formed. There are several sets of these amino acid-dependent, database-derived, statistical expectation values [59–63]. We choose to use the Forman-Kay protocol [64], which uses all backbone chemical shift values and calculates a combined secondary structure propensity (SSP) value between −1 and 1, where −1 is fully formed β-sheet, 0 is a random coil,

and 1 is fully formed α-helix. For leptin^{0Trp} (Fig. 2), we find four regions along the sequence with fully formed α-helices and one region with a partly formed helix (residues 106−115). Comparing the SSP data from the combined chemical shifts with the crystal structure (Fig. 2), we find that the positions and edges of the fully formed helices overlay very well with helices a, b, c, and d in the crystal structure (Fig. 2). However, the region corresponding to helix 4' (Fig. 2) does not show fully formed helix, but rather SSP values around 0.5, indicating that the helix is formed only a fraction of the time [65,66], i.e., at any given time point approximately 50% of the leptin molecules contain helix 4'. This means that helix 4' is transiently formed and only meta-stable [67]. We can also conclude that helix 4' is in fast exchange with a coiled state, i.e., fast on an NMR timescale, as we do not find a double set of cross-peaks for any residues in helix 4' (although a couple of the cross-peaks are split, we assign this to other events, *see further below*). This conclusion is also based on the fact that the chemical shifts reported are between the expected values of a stable helix and that for a random coil, i.e., the observed position is the population-weighted value in fast exchange [68,69]. In the crystal structure, nevertheless, the helix seems to be fully formed, with low B-factors and no clear alternative structures. This suggests that helix 4' is favorably packed in the crystal lattice [34]. Such transient helices are likely to play an important functional role, putatively in primary receptor binding [65,70,71], or secondary bridging of the receptor monomers.

In the crystal structure, there are two relatively long disordered loops, comprising residues 24−51 and 94−105 that we in the following call loop I and loop III (Fig. 2). In both loops, we find negative SSP values,

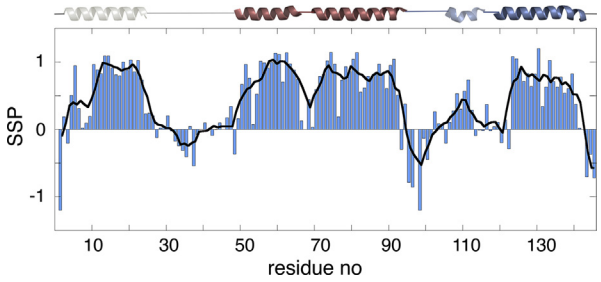

Fig. 2. The secondary structure propensity (SSP) calculated from NMR chemical shifts. The positioning of the helical elements, with the same color code as in Fig. 1, along the primary sequence, is shown above the SSP panel. The SSP value is 1 for fully formed helix and −1 for fully formed β-strand. The solution state helices seem to perfectly overlap with those in the crystal structure. Helix 4' shows a lower SSP value than helices a-d, indicating a transient structure, with only partly populated helix at any given time point.

indicating extended or β-sheet content [64]. In loop I, the values are relatively modest while loop III shows SSP values close to −1. In the crystal structure, loop I is not visible and is flanked by elevated B-factors (Supporting Fig. S2), suggesting a dynamic loop with no single structural state. This is in line with the SSP data that suggest a merely transiently adopted or no secondary structure. On the other hand, loop III shows electron density along the whole loop, with slightly elevated B-factors (Supporting Fig. S2). This suggests a relatively ordered, extended loop flanking the surface of leptin^{0Trp}. This extendedness should correspond to dihedral angles typical for β-sheets. From the crystal structure [34] the dihedral angles φ and ψ can be calculated and in a Ramachandran-plot representation loop I residues show dihedral angles distributed in all allowed regions, while residues in the extended part of loop III show dihedral angles that are clustered in the extended sheet region (Supporting Fig. S3). The extended loop can be depicted as structurally strained, or "forced" into dihedral angles that resembles those of a β-sheet [64,72,73], yielding secondary chemical shifts corresponding to the partial β-sheet formation. The chemical shift data suggest that the solution structure is well represented by the crystal structure [34], and as per the following, we assume the structure to be correct and use NMR to further investigate the dynamic properties of leptin.

A minor structural state in slow exchange

A subset of the cross is split in two, where one corresponds to a weakly populated state (Fig. 3). The minor population estimated from the peak volume is approximately 20%. These doublet peaks indicate the presence of two structural states in slow exchange. While the minor population does not have sufficient signal-to-noise to be unambiguously assigned, the pattern indicates that most of the resonances are just slightly shifted (Fig. 3), which, in turn, suggests that the minor state is similar to the ground state. Fig. 3 shows how the split peaks align with the structure. Interestingly, the residues that undergo this slow exchange cluster in a region involving helices b and 4', and loop III, which are neighboring in the crystal structure. Notably, there is a proline at position 99 in loop III. A straightforward interpretation of the split peaks would be proline isomerization, with a slightly varied packing of helix 4' onto helix b when P99 is in the *cis*-conformation or in the *trans*-conformation. This packing malleability may be of functional importance as this proline is conserved [33].

Leptin^{0Trp} has several prolines (P43, P47, P69, P99, and P144), and the second cluster of split cross-peaks suggest long-range inter-residue contacts with P144, although this proline is in a relatively tight loop (Fig. 3). This cluster involves the actual

threading region, i.e., the region that crosses under the disulfide formed loop and residues 49–52 (Fig. 3), and maybe due to two conformations of P144. On the other hand, P43 and P47, located in loop I, show no detectable alternative conformations, i.e., the surrounding cross-peaks appear as single peaks. From the $^{13}C^{\beta}$ chemical shifts all prolines [74], save P47, are in *cis*-conformation (SI, Table S1), fully in agreement with the crystal structure.

The helices a-d constitute a framework with well-defined helices, while the loop I, loop III, and helix 4' constitute a structurally less well-defined domain. Such dynamic functional regions can typically be found in soluble proteins involved in protein-protein interactions [65,70,71]. However, from the chemical shift analysis we only have indirect dynamical information. In order to obtain direct dynamical information, we opted for NMR relaxation measurements.

Leptin^{0Trp} shows rotational diffusion behavior corresponding to a folded monomer

NMR relaxation can be used to obtain both general and specific information on molecular motions and dynamics, which provide us with a tool to further benchmark the properties of soluble leptin^{0Trp}. In order to map out the dynamics of leptin^{0Trp}, we determined the ^{15}N relaxation rates R_1 and R_2, as well as the cross-relaxation rates (σ_{NH}) reflected in the nuclear Overhauser effect (NOE) (Fig. 4). Plotting R_1/R_2 and cross relaxation (Fig. 5) as a function of sequence position provides information on the dynamic behavior of leptin^{0Trp}, and shows that the helical core (helix a-d), behaves as expected for a well-defined globular protein, while there are two regions, corresponding to loops I and III that show increased fast timescale dynamics, suggesting a more disordered state of the loops. The R_2/R_1 ratio can be used to quantitatively estimate the overall rotational correlation time of leptin^{0Trp}, given that R_2/R_1 values from residues in fast motion regions are omitted [75]. From the determined relaxation rates, we estimate the rotational correlation time to be $\tau_c = 9.2 \pm 0.2$ ns when omitting relaxation data from loops I and III and the N- and C-termini. The determined rotational correlation time corresponds to a 15.1 kDa protein from the linear correlation between rotational correlation time and molecular weight [76]. This is in reasonable agreement with leptin^{0Trp}'s theoretical $M_w = 15.8$ kDa, and the slightly lower experimental value indeed underlines that leptin^{0Trp} seems to be monomeric in solution at 100 μM concentration. The slight offset can stem from protein-specific variability in the linear relationship, due to e.g. shape factors [77]. An alternative method to evaluate the rotational correlation time is to calculate the hydrodynamic radius (R_H) from Stoke's law and compare it with the expected R_H from the relationship $R_H = 1.13M_w^{0.3}$ [78], derived from translational diffusion measurements. From Stoke's law, we obtain $R_H = 21.6$ Å, while the expected hydrodynamic radius calculated from the mass is 20.6 Å, in good agreement. We can conclude that leptin^{0Trp} is monomeric in its free soluble form and that it shows all the characteristics of a folded, well-defined protein. However, relaxation data do not only report on the global properties of the protein but can also reveal detailed information with atomic resolution [50,79].

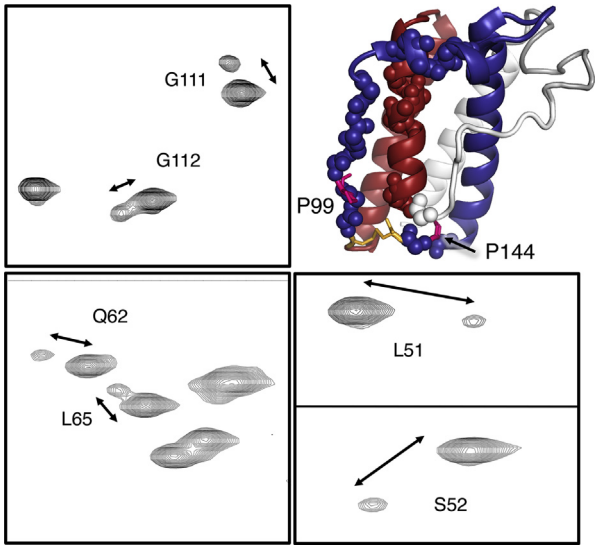

Fig. 3. A subset of the cross peaks in the TROSY spectrum shows cross-peak splitting, with a low populated secondary state in slow exchange with the dominating state. A couple of representative split peaks are shown. Most of these split peaks cluster in the structure, e.g., involving the packing of helix 4' to the protein body, as well as the threading region of the lasso topology. The residues with split peaks are highlighted as spheres in the structure figure. The splitting may stem from proline (magenta) isomerization from both sides of the pierced lasso, forming a disulfide bond (yellow).

NMR relaxation data suggests some degree of order in loops I and III

A combined analysis of all relaxation parameters can provide additional detailed structural and dynamic information of leptin^{0Trp}. The well-defined helices a-d seem to constitute a relatively rigid frame for the protein (Fig. 5), especially highlighted by the slow timescale dynamics. From the presented NMR relaxation data, we can conclude that the two long loops, loops I and III, show increased local dynamics, compared to the helical frame, on all timescales. The fast timescale dynamical pattern from NOE data agrees well with *in silico* data, also

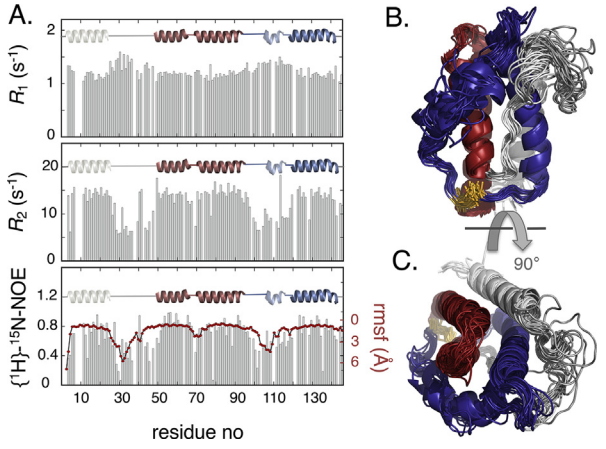

Fig. 4. The individual relaxation parameters, R_1, R_2, and steady-state NOE, shown in (A), again exhibit a pattern with dynamic loops anchored to a rigid fold. The R_2 and NOE values show that the central region of loop I is strongly anchored to the secondary loops, making this region relatively rigid. The positioning of the helical elements along the primary sequence is shown above each panel. Bottom panel in (A): Local conformational dynamics from molecular dynamics simulations are strongly correlated to *in vitro* NOE measurements. Regions of high NOEs generally have low rmsf in the simulated ensemble, and regions of low NOEs have high rmsf. Exceptions are the C-terminal region of loop I and the N-terminal region of loop III, which are relatively more stable in the simulations than in the *in vitro* measurements. Note that since rmsf and NOEs are inversely related, the ordinates are plotted in opposing directions to visually emphasize the relationship. In (B) and (C) a representative ensemble of structures from the MD-simulation is shown to visualize the location and amplitude of the loop dynamics, the color-coding is as in Fig. 1. Helix 4' is only formed in a subset of the ensemble, underlining the transient nature of this helix.

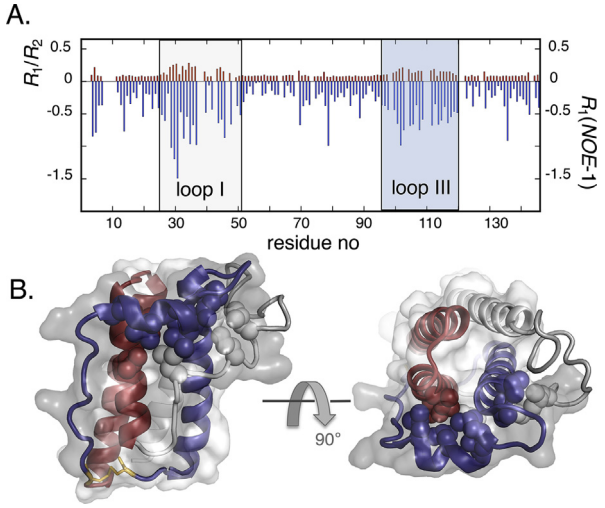

Fig. 5. NMR relaxation data show that the four helices in the protein body behave as a well-defined globular protein shown with low R_1/R_2 values and low magnitude R_1(NOE-1) values, while the long loops I and III are significantly more dynamic (A). In (B) the colocalization of the dynamic loops into a dynamic domain is shown as a grey shadowed surface. However, the presence of a secondary hydrophobic core leads to a somewhat lower degree of motions of the loops than anticipated from their length. The residues constituting the secondary hydrophobic core are shown as spheres.

reporting on ns dynamics. (Fig. 4). However, the loops also exhibit some local features that become more evident in the original unprocessed relaxation data. In Fig. 4, R_1, R_2, and NOE for the individual residues are shown, and it is clear that the long loops are not monotonically dynamic, i.e., the loops are not just anchored in the helices with increasingly unrestricted motions toward the center of the loops. In particular, loop I can, from R_2 and NOE data, be divided into dynamical segments. The initial residues 28–30 seem to be highly dynamic and show characteristics of a relaxed loop [80,81]. This is in agreement with crystallographic data, where this loop does not show any electron density, indicative of a dynamic loop [34]. On the other hand, the rest of loop I is less dynamic, with NOE values around 0.5 suggesting more restricted motions. This may be due to the fact that this loop is packed onto the protein surface [34], or alternatively packed against a transiently or fully formed structural element. The SSP analysis of this region shows values shifted toward β-sheet content, which may suggest a β-hairpin in loop I. The lack of electron density in this region [34] then may reflect heterogeneous packing of a putative structural element or fast, free dynamics. Indeed, the apparent flexibility of the N-terminal half of loop I agrees with the large root-mean-squared fluctuations (rmsf) of residues 24–42 in all-atom simulations (Fig. 4). It must be pointed out that due to the lack of electron density, the simulations were initialized using a reconstructed loop region 25–38 using the template-based loop structure prediction sever ArchPRED [82], which initially biases the region to a loop structure. Loop III, harboring the transient formed helix 4', shows a more rigid behavior than loop I. The average NOE is 0.56 ± 0.12, which is significantly higher than expected for a disordered loop of that length. As an example, the disordered functional loop IV in SOD1, of similar length, shows an average NOE of 0.27 [80]. This indicates that loop III in leptin^{0Trp} is dynamically restricted, in line with the presence of a transient helix (Fig. 2). Nevertheless, the transient helix 4' is very dynamic, and the clear helical signature found in the SSP analysis is not as clear in the relaxation data (Figs. 2, 4 and 5). The C-terminus show relaxation rates corresponding to a

high degree of rigidity, due to its anchoring to loop III. This dynamic signature of an LPT is then crucially dependent on the oxidative state of leptin, and a reduction of the intramolecular disulfide bond would render a very different dynamic, and putatively functional profile of leptin.

Leptin^{0Trp} has a secondary hydrophobic core, anchoring the long-disordered loops

We can conclude that the long loops show slightly lower mobility than expected for random loop structures. In the center of loop I, there are a couple of residues showing relaxation properties similar to the helical frame, D40 to I42 (Fig. 4). A clue to the reason for this unusual behavior can be found in the crystal structure [34]. The hydrophobic sidechains, L39, I42, and L45, pack into a secondary hydrophobic core on the side of the helical frame (Fig. w). This ties the center of the loop onto the body of the protein, which may result in more restricted dynamics. The B-factors of this central rigid part of loop I are similar to those in the helices (Supporting Fig. S2), supporting the hypothesis that the loop may anchor to the secondary hydrophobic cluster. Additionally, all-atom simulations predict specific structure between loop I and loop III that is largely missing from the crystal structure. The loop I structural ensemble has elevated rmsf while maintaining several specific contacts with loop III/helix d (Fig. 4 and Supporting Fig. S4), consistent with a dynamic hydrophobic packing. The relaxation data suggest that the C-terminal region of loop I (residues 43–50) is more flexible. In contrast, all-atom simulation suggests that the C-terminal half of loop I is stable near the crystal configuration (Fig. 4), showing a relatively rigid turn connecting loop I and helix b. In loop III only a single residue, L114, shows relaxation rates corresponding to a more rigid conformation. In line with this, L114 has a lowered B-factor ([34], Supporting Fig. S2). The dynamical signature of helix 4', underlines the transient nature of the formed helix, however, similar to the center of loop I, loop III is dynamically restricted in its central part, probably independent on the structural state of helix 4'. All-atom simulations qualitatively agree, showing elevated rmsf for all of loop III apart from residues L114/E115 (Fig. 4). The loops, taken together, seem to be anchored into a secondary hydrophobic core (Fig. 5). The major hydrophobic core is located in the interior of the protein, packing the frame helices to its native four-helix bundle conformation [34]. Outside of this, on the surface of the protein, leptin^{0Trp} has a secondary hydrophobic core formed by residues in helices b, 4'and d, and loop I (Fig. 5). The secondary core seems to be relatively well-defined, even though it is located in a dynamic region, as several of the anchoring points are rigid and probably long-lived (Figs. 4 and 5).

Mapping out the dynamic regions along the sequence, i.e., loops I and III, on the leptin^{0Trp} structure (Fig. 5C) show that they co-locate and constitute a dynamic domain. It is attractive to hypothesize that this dynamic domain is functional and is involved in receptor recognition, binding and/or allosteric signaling. Such functional plasticity has been shown in numerous systems [65,70,71]. Leptin has been suggested to have three binding sites [12–16] (binding site I, II and III) for binding to the leptin-receptor where site III is located in the dynamic domain (loop I and III), while site II is located on the opposite, more rigid region of leptin (helices a and c) (Fig. 1). This pattern may suggest a dynamic allosteric coupling between the two binding sites, which could be critically dependent on the dynamic nature of loops I and III. Furthermore, the loops seem coordinated into a pre-organized state by the core anchors, which support its functional role. This would then give the functional plasticity but reduce the entropic cost of ordering upon binding. In some systems, the disordered dynamic regions have a tendency to adopt the active state, also without any putative binding partner, in so-called "selective fit models" [83]. These pre-existing binding competent conformations are typically low in population and in fast to intermediate exchange with the disordered ground state [84]. To test if leptin^{0Trp} undergoes such chemical exchange on an intermediate timescale (μs-ms) we performed relaxation dispersion measurements that can be utilized to quantify both the thermodynamics and the kinetics on an exchange between two chemically distinct states in exchange on a favorable timescale [85]. However, no relaxation dispersion profiles were detected, indicating that the motions in the dynamical domain are predominantly in the fast regime, at least without the native receptor ligand. We conclude that the secondary core coordinates a dynamical domain of leptin^{0Trp} (Fig. 5C), and the transient helix 4' is part of a putative functional dynamical structural state. However, we have no direct experimental data on the lifetime of any structural states in the dynamical domain, so to be able to estimate a lower limit on the lifetime, we measured the amide hydrogen-deuterium exchange (HD-exchange) rates using NMR spectroscopy.

HD-exchange measurements confirm the dynamic domain

A well-established method to observe local and global structural lifetimes in the native state is a hydrogen-deuterium exchange of the protein backbone amide protons [86]. The method ensures that amide hydrogens are protected from exchange with solvent when involved in stable hydrogen bonds. To quantify the exchange rate for each amide proton, we diluted a concentrated NMR sample with a D_2O-

based buffer and measured the exchange-induced signal decay for each observable cross peak. The logarithm of the observed signal decay rates is shown in Fig. 6A, where the majority of all cross peaks have fully or almost fully exchanged during the experimental dead time, i.e., from dilution to first NMR spectrum (2 min). Only 42 amides show some degree of protection (Fig. 6), and most of these show slow exchange rates, with $\log k_{ex}^{obs} < -3$. (where the units of the rate constants are in s^{-1}). The regions with slow exchange correspond to helices a-d, and the absence of protected amides in the 105−115 region underlines the dynamic and transient nature of helix 4'; all amides have exchanged during the experimental dead time. Furthermore, no protection is found in the loop regions, even though they show reduced motional freedom (Figs. 4 and 5). We find only one amide, C96, outside the helical cores, which shows protection from the solvent exchange that is part of the disulfide bridge maintaining the PLT intact. In the crystal structure, the amide of C96 forms a hydrogen bond with A91. Interestingly, the protection increases toward the center of the helices, suggesting a stable, rigid band, keeping helices a-d together, similar, as found for β-barrels [80]. The ends of the helices show less pronounced protection, indicating some degree of movement freedom and transient hydrogen bond breakage, although relaxation data indicates that on fast timescales (pico-to nanoseconds), these regions are rigid.

Taken together, the HD-exchange pattern (Fig. 6A−B) suggests detectable amide proton exchange upon global unfolding, given a two-state cooperative behavior, typical for small, single-domain proteins [52,86,87]. The exchange rates in the center of the helices, $\log k_{ex}^{obs} < -3$, could then reflect the global unfolding rate if in the EX1 regime. This would be a relatively slow unfolding rate for an all-helical protein, and more likely, the exchange rate is in the EX2 regime. To address this issue, we measured the folding kinetics experimentally.

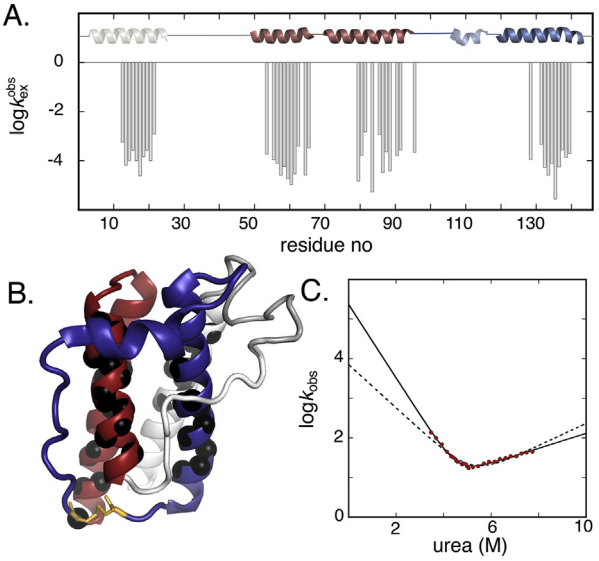

Fig. 6. (A) The logarithm of the amide proton exchange rate (in s^{-1}) from HD-exchange data shows that helices a-d exhibit amide proton protection that is limited by global unfolding kinetics, in the EX2 regime. No protection is found in the transient helix 4'. The positioning of the helical elements along the primary sequence is shown as an inset. In (B) the location of protected amide protons are shown as black spheres. The majority is located in the central parts of the helices, in line with an increased native state dynamic toward the helical ends. (C) The folding kinetics of leptin. The free fitted folding rate is shown as a solid line, while the expected folding rate from HD-exchange and Eq. (1), is shown as a dashed line. The chevron plot has all the characteristics of a two-state folding protein, although the refolding limb is relatively short, which indeed introduce uncertainties in the extrapolated folding rate, and obscures any putative curvatures in the urea dependence of the refolding rate.

Kinetic analysis shows that HD-exchange occurs in the EX2 regime

The folding kinetics was studied on the W100E leptin variant (leptin^{pwt}) instead of leptin^{0Trp}, in order to have one fluorescently active tryptophan in the protein to report on the folding process. The stopped-flow analysis shows all the characteristics of a two-state cooperative folding transition [88], with no observed additional minor relaxation phases. The urea dependence of the logarithm of the folding ($\log k_u$) and unfolding ($\log k_u$) rates are linear in the observable urea-range and show a typical v-shaped chevron plot (Fig. 6) The folding rate is very fast, and for urea concentrations below 3.4 M the rate is too fast to be reliably determined in the stopped-flow apparatus. The parameters obtained from the kinetic data are listed in Table 1. The *m*-value, the derived transition mid-point (MP^{kin}) and the free energy between the folded and unfolded state are all in excellent agreement with the corresponding value from equilibrium titration data (Table 1, Supporting Fig. S5) [35]. The refolding limb of the chevron plot is only defined by a few data points, which results in some uncertainty in the extrapolated $\log k_u$ value. Nevertheless, the free energy difference between folded and unfolded leptin determined from the extrapolated k_u and k_f is very similar to the value from the equilibrium titration data (Fig. 6 and Table 1). Interestingly, the protein stability found here, for leptin^{wt} (equilibrium data) and leptin^{pwt} (kinetic data) are both significantly more stable than reported earlier [35]. In the previous study, leptin^{pwt} stability was determined by guanidinium chloride titration, an experiment with a high ionic strength that may shift the stability [35].

The pattern of exchange protection (Fig. 6) shows that, in general, the centers of the helices are more protected than the edges, which is typical of globular proteins. This is a direct result of native state dynamics, where the hydrogen bonds in the helical edge regions transiently break and reform, in the native state basin, resulting in exchange without global unfolding [87]. In leptin, the helices show relatively uniform exchange rates, save helix c that shows variability (Fig. 6). This suggests that helix c exhibits more ground state dynamics, although relaxation measurements reveal no increased fast motions (Fig. 4). The B-factors in the crystal structure [34] are also uniformly low in helix c. This indicates that, although relatively rigid and well defined in the native state, rare fluctuations (less frequent than a nanosecond, but faster than seconds) occur in helix c occurs, causing increased HD-exchange rates. The two residues within the protected region of helix c that show low protection N82 and L86 are directly linked by the $i+4$ hydrogen bond, i.e., the slow timescale dynamics in the center of helix c seems correlated and involve probably concerted H-bond breakage (Supporting Fig. S6), putatively due to helix bending.

The HD-exchange data can now be analyzed further, using the k_f and k_u values obtained from the kinetic analysis as k_{op} and k_{cl} in Eq. (1), and calculate the intrinsic exchange rates using the protocols of Englander and co-workers [89]. First, we conclude that the amide proton exchange of leptin^{0Trp} is in the EX2 regime, as $k_f \gg k_{ex}^{int}$ for all residues (Fig. 6, Table 1, Supporting Table S2). The observed HD-exchange data and the calculated values from Eq. (1) are listed in Supporting Table S2. It is evident that the observed rates are significantly faster than the predicted rates by more than a factor of ten for the majority of the protected residues (Supporting Fig. S7).

We identify several plausible explanations for this discrepancy: *(i)* the sequence difference in the leptin constructs used to collect NMR, kinetic and equilibrium data result in somewhat lowered refolding rates, or *(ii)* the extrapolated k_f is overestimated, *(iii)* ground state dynamics causes local structural integrity fluctuations. Explanation *(i)* reflects that the NMR study was performed on the double mutant W100E/W138E, kinetic measurements were performed on the single mutant W100E. Circular dichroism equilibrium denaturation measurements on the wild-type protein, the W100E and W100E/W138E variants show that the thermodynamic stability of all three leptin variants is similar with only moderate variation in $\Delta G_{U/F}$ and $m_{U/F}$-values (Supporting Information, Table S3 and Fig. S8). This is also in line with that the NMR spectra of the variants are very similar (Supporting Information, Fig. S1), indicating any significant structural differences. Overestimation of the refolding rate (*ii*), is possible as the value in Table 1 is derived from the extrapolation of a relatively few data points under the assumption that log$K_{U/F}$, as well as logk_f, are linearly dependent on [urea] (Fig. 6C). The amplitude of curvature needed to explain the discrepancy is significant, but not unusually large [90], as an example: U1A has both curved unfolding and refolding limbs, where the true logk_f is one log unit lower than the linearly extrapolated value [90]. Finally, structural native state fluctuations in the dynamic helical protein lead to transient hydrogen bond breakage and HD-exchange (explanation (*iii*)). Local transient unfolding is a typical feature of a helical secondary structure [91], as opposed to the structural integrity found in the tertiary defined β strand structures, where significant local breakage of H-bonds is typically associated with global unfolding [92].

Table 1. Kinetic and thermodynamic parameters of leptin^{pwt}. Rate constants are in units of s^{-1}.

$\log k_f^{H_2O}$ [a]	5.58 ± 0.20
$\log k_u^{H_2O}$ [a]	0.47 ± 0.06
m_f (M^{-1}) [a]	−0.99 ± 0.05
m_u (M^{-1}) [a]	0.15 ± 0.01
$m_{U/F}^{kin}$ (M^{-1}) [b]	1.14 ± 0.05
MP^{kin} (M) [c]	4.48 ± 0.27
$\Delta G_{U/F}^{kin}$ (kcal/mol) [d]	6.96 ± 0.29.
$m_{U/F}$ (M^{-1}) [e]	1.04 ± 0.04
MP^{eq} (M) [e]	4.82 ± 0.02
$\Delta G_{U/F}^{eq}$ (kcal/mol) [e]	6.9 ± 0.4

[a] Derived from fitting of kinetic data in Fig. 6.
[b] $m_{U/F} = m_u - m_f$.
[c] The transition midpoint derived from the intersect between $logk_f$ and $logk_u$ where [U] = [F].
[d] $\Delta G_{U/F}^{kin} = -2.3RT\,(logk_u^{H_2O} - logk_f^{H_2O})$.
[e] Derived from fitting equilibrium unfolding data in Supporting Fig. S5.

Concluding Remarks

In this study, we have, with high resolution, characterized the structural and dynamic properties of soluble leptin^{0Trp}, which will serve as a benchmark for future functional studies of leptin. Leptin^{0Trp} in solution behaves as a structurally well-defined monomeric protein with a seemingly low degree of large amplitude dynamics. The relaxation properties are in good agreement with a globular protein of this size, save for two regions corresponding to the two long loops, which exhibit a higher degree of mobility (Figs. 2, 4 and 5). Particularly interesting is the dynamic signature of the region where the pierced lasso anchors and where the actual threading takes place (Fig. 3). The slow dynamics stemming from the P99, P144, and disulfide cluster seem to transfer into the packing of the transient helix 4', as well as the precise threading through the covalent loop.

Interestingly, all prolines, save P47, adopt *cis*-conformation, although parts of dynamic loops. This underlines that the loops have some motional restriction that keeps the prolines in the less preferred conformation. Helix 4' (Fig. 2) is indeed transiently formed, but the exchange between folded and unfolded occurs on a much faster timescale and seems unrelated to the slow pierced lasso dynamics. Transient helices are often functional and helix 4' may be involved in leptin interaction with its receptor. Nevertheless, helix 4' is anchored to the protein body in a secondary core (Fig. 5), into which both loops I and III are also anchored. The relaxation data show reduced fast motions for the residues anchoring the secondary core to the helical frame, while the HD-exchange data, reporting on slow timescale dynamics, show no protection in this area. Thus, the transient nature of helix 4' is also valid for the surrounding secondary core. Finally, loops I and III, together with helix 4' build up a dynamic surface region, i.e., a dynamic domain (Fig. 5C). This dynamic region is most likely functional, which is underlined by the fact that loops I and III are highly conserved [15,33]. The anchoring of the loops should not only predispose the loops in a putatively functional state but also reduce the entropic cost of functional interactions, folding, and binding.

Methods

Protein engineering, expression, and protein purification

Leptin was cloned into a pET-3a vector and transformed into competent BL21(DE3) *E. coli* cells [35]. A single point mutation was introduced using the Quick-change site-directed mutagenesis kit (Stratagene). Oligonucleotides were purchased from Integrated DNA Technology. Sequence identity was confirmed by sequencing (ETON Bioscience Inc.) The W138E mutation (leptin^{0Trp}) was introduced to ensure monomeric protein in solution at concentrations used for NMR, as neither the naturally occurring protein (leptin^{wt}) or the leptin variant used for crystallization (leptin^{pwt}) remain monomeric at concentrations necessary for NMR assignment experiments (Supporting Information [34]).

Protein expression was induced by addition of 1 mM IPTG, and cells were harvested and purified from inclusion bodies as described in Ref. [35]. All samples were purified on a size exclusion column (Sephacryl-100 resin) after refolding to eliminate oligomeric/misfolded species. Protein purity was determined by SDS-PAGE, and leptin containing fractions were collected.

Nuclear magnetic resonance

The NMR assignment was carried out from a standard set of triple-resonance experiments: HN(CO)CACB [93], HNCACB [94], HNCO and HN(CA)CO [95] were all TROSY-based and used band selective excitation for fast acquisition (BEST) [56–58]. $^{1}H-^{15}N$-HSQC and HSQC-TROSY experiments were collected on a 950 MHz Bruker magnet equipped with a CryoProbe at 25 °C, using a 10 mM Mes buffer at pH 6.3 and 10% D_2O. The assignments are deposited in the BioMagResBank (access number 50004, http://deposit.bmrb.wisc.edu/author_view?BMRB/50004_hy_gkigpnjv.str).

Scheme 1. HD-exchange occurs upon exposure of an closed amide proton (C) due to breakage of a hydrogen bond to an open state (O).

H/D-exchange analysis

H/D-exchange data were collected on a 600 MHz Bruker magnet equipped with a CryoProbe at 25 °C, using a 50 mM BisTris buffer at pH 6.3 and with a final concentration of >50% D_2O. The final protein concentration was 100 μM, for all experiments. The experimental dead time (i.e., the sample preparation and experiment setup) was 2 min, and SOFAST-HMQC spectra were recorded every minute for the first hour, then every 5 min from 1 to 5 h, then every 15 min from 5 h to 11 h and finally every hour to 66 h. The attenuation of the signal intensity (peak height) due to exchange was fitted to a single exponential decay. While protected in a hydrogen bond, the amide is assigned to be in a closed state (C). If the hydrogen bond is broken, the amide is exposed and can interact with solvent D_2O to exchange the proton to a deuteron (see Scheme 1). The exchange is preceded by breakage of a hydrogen bond to an open state (O), as follows:where k_{op} and k_{cl} are the opening and closing rates of the hydrogen bond, and k_{ex}^{int} is the pH and temperature-dependent intrinsic exchange rate of the amide proton in the open state [86,87,89]. The observed HD-exchange rate is then:

$$k_{ex}^{obs} = k_{op} k_{ex}^{int} / \left(k_{op} + k_{cl} + k_{ex}^{int}\right) \approx k_{op} k_{ex}^{int} / \left(k_{cl} + k_{ex}^{int}\right) \quad (1)$$

where $k_{op} \ll k_{cl}$ for a stable protein. If every opening event is likely to result in exchange ($k_{cl} < k_{ex}^{int}$), the system is in the EX1 regime and Eq. (1) simplifies to, $k_{ex}^{obs} = k_{op}$ [87]. If, on the other hand, the hydrogen bond closes with a rate faster than the intrinsic rate ($k_{ex}^{int} < k_{cl}$), only a fraction of the opening events results in exchange. This is the EX2 regime and Eq. (1) is simplified to $k_{ex}^{obs} \approx k_{ex}^{int}(k_{op}/k_{cl}) = K_{O/C} k_{ex}^{int}$ [87].

Kinetic measurements

The kinetic measurements, as shown in Fig. 6C and Table 1, were obtained from intrinsic tryptophan fluorescence, collected on an SX19 stopped-flow apparatus

equipped with an LED light source from Applied Photophysics. The excitation wavelength was 280 nm, and emission was collected with a 305-nm cut-off filter. Buffers used were 10 mM MES at pH 6.3 with urea concentrations between 0 and 10 M. All measurements were at 25 °C, and the final protein concentration was 3 μM. The data were fitted according to the two-state equation:

$$\begin{aligned}\log k_{obs} &= \log\left(k_f + k_u\right) \\ &= \log\left(10^{\log k_f^{H2O} + m_f[\text{urea}]} + 10^{\log k_u^{H2O} + m_u[\text{urea}]}\right)\end{aligned} \quad (2)$$

where k_f^{H2O} and k_u^{H2O} are the extrapolated values of the refolding (k_f) and unfolding (k_u) rate constants at 0 M urea, and m_f and m_u are the slopes of the urea dependence of the logarithm of refolding and unfolding rates, respectively.

Equilibrium experiments

Fluorescence equilibrium data were collected using a Chirascan V100 Circular Dichroism spectrometer from Applied Photophysics using a 10 mm cuvette. The excitation was at 280 nm, and emission spectra were collected between 300 and 500 nm. Buffers used were 10 mM MES at pH 6.3, with urea concentrations between 0 and 8 M. All measurements were at 25 °C, and the final protein concentration was 0.1 mg/ml.

Equilibrium circular dichroism experiments

CD equilibrium data were collected using a Chirascan V100 Circular Dichroism spectrometer from Applied Photophysics using a 1.0 mm cuvette. Circular dichroism spectra were collected between 200 and 240 nm. The folding transition was recorded by the signal at 222 nm. Buffers used were 10 mM MES at pH 6.3, with urea concentrations between 0 and 8 M. All measurements were at 25 °C, and the final protein concentration was 0.1 mg/ml. Data were fitted to:

$$S_{OBS} = S_F + k_f[\text{urea}] + \frac{S_U + k_U[\text{urea}]}{1 + e^{\frac{-\Delta G_{U/F}}{RT}}} \quad (3)$$

Where $S_x + k_x$[urea] correspond to the sloping baselines, ΔG is the free energy difference between the folded and unfolded state, R is the gas constant and T the temperature.

Molecular dynamics (MD) simulations

Explicit solvent simulations for leptin were performed with the Gromacs 5.0.4 [96] on a BlueGene/Q supercomputer using the Amber99-ILDN protein forcefield [97] and TIP3P water. A 61 Å cubic box contained 23,078 atoms. Three sodium atoms were added to neutralize the system, additional NaCl was added to bring the salt concentration to 0.1 M, and PME electrostatics was used with a Fourier spacing of 1.2 Å. An NPT ensemble was implemented by v-rescale and a Berendsen barostat for a temperature of 300 K and a pressure of 1 bar. Hydrogens were constrained with LINCS, and the time step was 2 fs. The total simulation time was 1.5 μs, which included an initial 200 ns of equilibration and 1.3 μs of production that was analyzed to produce the presented ensemble averages. Root-mean-squared fluctuations were calculated using the structure after the equilibration as the reference.

Acknowledgements

The research was funded by the Knut and Alice Wallenberg Foundation (2017−0041), the Swedish Research Council (2017−01517), and the Magnus Bergvall Foundation (2017−02228). This work has also been supported by iNEXT, grant number 653706, funded by the Horizon 2020 program of the European Commission. Additionally, this work was supported by the Center for Theoretical Biological Physics sponsored by the NSF (Grant PHY-1427654 and CHE-1614101). JNO is a Cancer Prevention and Research Institute of Texas (CPRIT) Scholar in Cancer Research. We acknowledge the generous support provided by the Rice University BlueGene/Q supercomputer. Ellinor Haglund is supported in part by the Welch Foundation (Grant C-1792). Work at UCSD was supported by the NSF (Grant PHY-1614407). We wish to thank Christian Richter and Frank Löhr for valuable help with NMR instrumentation at Johann Wolfgang Goethe Universität in Frankfurt.

Author contributions

Jens Danielsson, Data curation, Formal Analysis, Project Administration, Methodology, Investigation, Original Draft, Review & editing. *Jeffery K. Noel,* Data curation, Formal Analysis, Methodology, Investigation, Review & editing. Jennifer M. Simien, Data curation. *Brendan Duggan*, Data curation, Methodology, Investigation, Formal Analysis, Review & editing. *Mikael Oliveberg*, Funding acquisition, Supervision, Review & editing. *José N. Onuchic*, Funding acquisition, Supervision, Review & editing. *Patricia A. Jennings*, Funding acquisition, Supervision, Review & editing. *Ellinor Haglund*, Conceptualization, Data curation, Funding acquisition, Formal Analysis, Methodology, Investigation, Project Administration, Review & editing.

Appendix A. Supplementary data

Supplementary data to this article can be found online at https://doi.org/10.1016/j.jmb.2020.01.035.

Received 12 September 2019;
Received in revised form 18 January 2020;
Accepted 24 January 2020
Available online 17 February 2020

Keywords:
conformational dynamics;
NMR;
protein folding;
obesity;
leptin

References

[1] H.P. Weingarten, Stimulus control of eating: implications for a two-factor theory of hunger, Appetite 6 (1985) 387–401.
[2] Y. Zhang, R. Proenca, M. Maffei, M. Barone, L. Leopold, J.M. Friedman, Positional cloning of the mouse obese gene and its human homologue, Nature 372 (1994) 425–432.
[3] P.G. Cammisotto, M. Bendayan, Leptin secretion by white adipose tissue and gastric mucosa, Histol. Histopathol. 22 (2007) 199–210.
[4] G.H. Lee, R. Proenca, J.M. Montez, K.M. Carroll, J.G. Darvishzadeh, J.I. Lee, et al., Abnormal splicing of the leptin receptor in diabetic mice, Nature 379 (1996) 632–635.
[5] H. Chen, O. Charlat, L.A. Tartaglia, E.A. Woolf, X. Weng, S.J. Ellis, et al., Evidence that the diabetes gene encodes the leptin receptor: identification of a mutation in the leptin receptor gene in db/db mice, Cell 84 (1996) 491–495.
[6] R.L. Londraville, J.W. Prokop, R.J. Duff, Q. Liu, M. Tuttle, On the molecular evolution of leptin, leptin receptor, and endospanin, Front. Endocrinol. 8 (2017) 58.
[7] T. Murakami, T. Yamashita, M. Iida, M. Kuwajima, K. Shima, A short form of leptin receptor performs signal transduction, Biochem. Biophys. Res. Commun. 231 (1997) 26–29.
[8] A. Di Spiezio, E.S. Sandin, R. Dore, H. Müller-Fielitz, S.E. Storck, M. Bernau, et al., The LepR-mediated leptin transport across brain barriers controls food reward, Mol. Metab. 8 (2018) 13–22.
[9] F. Langlet, A. Mullier, S.G. Bouret, V. Prevot, B. Dehouck, Tanycyte-like cells form a blood-cerebrospinal fluid barrier in the circumventricular organs of the mouse brain, J. Comp. Neurol. 521 (2013) 3389–3405.
[10] A. Mullier, S.G. Bouret, V. Prevot, B. Dehouck, Differential distribution of tight junction proteins suggests a role for tanycytes in blood-hypothalamus barrier regulation in the adult mouse brain, J. Comp. Neurol. 518 (2010) 943–962.
[11] E. Balland, V. Prévot, [Tanycytes gate leptin transport into the hypothalamus], Med. Sci. 30 (2014) 624–627.
[12] L.V. Mancour, H.N. Daghestani, S. Dutta, G.H. Westfield, J. Schilling, A.N. Oleskie, et al., Ligand-induced architecture of the leptin receptor signaling complex, Mol. Cell 48 (2012) 655–661.
[13] K. Moharana, L. Zabeau, F. Peelman, P. Ringler, H. Stahlberg, J. Tavernier, et al., Structural and mechanistic paradigm of leptin receptor activation revealed by complexes with wild-type and antagonist leptins, Structure 22 (2014) 866–877.
[14] F. Peelman, K. Van Beneden, L. Zabeau, H. Iserentant, P. Ulrichts, D. Defeau, et al., Mapping of the leptin binding sites and design of a leptin antagonist, J. Biol. Chem. 279 (2004) 41038–41046.
[15] F. Peelman, L. Zabeau, K. Moharana, S.N. Savvides, J. Tavernier, 20 years of leptin: insights into signaling assemblies of the leptin receptor, J. Endocrinol. 223 (2014) T9–T23.
[16] B. Carpenter, G.R. Hemsworth, Z. Wu, M. Maamra, C.J. Strasburger, R.J. Ross, et al., Structure of the human obesity receptor leptin-binding domain reveals the mechanism of leptin antagonism by a monoclonal antibody, Structure 20 (2012) 487–497.
[17] A. Strobel, T. Issad, L. Camoin, M. Ozata, A.D. Strosberg, A leptin missense mutation associated with hypogonadism and morbid obesity, Nat. Genet. 18 (1998) 213–215.
[18] M. Wabitsch, J.B. Funcke, B. Lennerz, U. Kuhnle-Krahl, G. Lahr, K.M. Debatin, et al., Biologically inactive leptin and early-onset extreme obesity, N. Engl. J. Med. 372 (2015) 48–54.
[19] M. Wabitsch, L. Pridzun, M. Ranke, J. von Schnurbein, A. Moss, S. Brandt, et al., Measurement of immunofunctional leptin to detect and monitor patients with functional leptin deficiency, Eur. J. Endocrinol. 176 (2017) 315–322.
[20] L. Niv-Spector, M. Shpilman, A. Grupi, A. Gertler, The obese phenotype-inducing N82K mutation in human leptin disrupts receptor-binding and biological activity, Mol. Genet. Metabol. 100 (2010) 193–197.
[21] C.T. Montague, I.S. Farooqi, J.P. Whitehead, M.A. Soos, H. Rau, N.J. Wareham, et al., Congenital leptin deficiency is associated with severe early-onset obesity in humans, Nature 387 (1997) 903–908.
[22] B.C. Moon, J.M. Friedman, The molecular basis of the obese mutation in ob2J mice, Genomics 42 (1997) 152–156.
[23] N. Boute, V. Zilberfarb, L. Camoin, S. Bonnafous, Y. Le Marchand-Brustel, T. Issad, The formation of an intrachain disulfide bond in the leptin protein is necessary for efficient leptin secretion, Biochimie 86 (2004) 351–356.
[24] M.K. Chekhranova, S.K. Karpova, S.B. Iatsyshina, A. Pankov Iu, [A new mutation c.422C>G (p.S141C) in homo- and heterozygous forms of the human leptin gene], Bioorg. Khim. 34 (2008) 854–856.
[25] I. Mazen, M. El-Gammal, M. Abdel-Hamid, K. Amr, A novel homozygous missense mutation of the leptin gene (N103K) in an obese Egyptian patient, Mol. Genet. Metabol. 97 (2009) 305–308.
[26] C.J. Hong, P.J. Tsai, C.Y. Cheng, C.K. Chou, H.F. Jheng, Y.C. Chuang, et al., ENU mutagenesis identifies mice with morbid obesity and severe hyperinsulinemia caused by a novel mutation in leptin, PloS One 5 (2010), e15333.
[27] W. Fatima, A. Shahid, M. Imran, J. Manzoor, S. Hasnain, S. Rana, et al., Leptin deficiency and leptin gene mutations in obese children from Pakistan, Int. J. Pediatr. Obes. : IPJO : Off. J. Int. Ass. Stud. Obes. 6 (2011) 419–427.
[28] S. Saeed, T.A. Butt, M. Anwer, M. Arslan, P. Froguel, High prevalence of leptin and melanocortin-4 receptor gene mutations in children with severe obesity from Pakistani consanguineous families, Mol. Genet. Metabol. 106 (2012) 121–126.
[29] S. Thakur, A. Kumar, S. Dubey, R. Saxena, A.N. Peters, A. Singhal, A novel mutation of the leptin gene in an Indian patient, Clin. Genet. 86 (2014) 391–393.
[30] M. Wabitsch, J.B. Funcke, J. von Schnurbein, F. Denzer, G. Lahr, I. Mazen, et al., Severe early-onset obesity due to

bioinactive leptin caused by a p.N103K mutation in the leptin gene, J. Clin. Endocrinol. Metabol. 100 (2015) 3227–3230.
[31] A.S. Altawil, H.A. Mawlawi, K.A. Alghamdi, F.F. Almijmaj, A novel homozygous frameshift mutation in exon 2 of LEP gene associated with severe obesity: a case report, Clin. Med. Insights Pediatr. 10 (2016) 115–118.
[32] H. Yupanqui-Lozno, R.A. Bastarrachea, M.E. Yupanqui-Velazco, M. Alvarez-Jaramillo, E. Medina-Méndez, A.P. Giraldo-Peña, et al., Congenital leptin deficiency and leptin gene missense mutation found in two Colombian sisters with severe obesity, Genes 10 (2019).
[33] E. Haglund, L. Nguyen, N.P. Schafer, H. Lammert, P.A. Jennings, J.N. Onuchic, Uncovering the molecular mechanisms behind disease-associated leptin variants, J. Biol. Chem. 293 (2018) 12919–12933.
[34] F. Zhang, M.B. Basinski, J.M. Beals, S.L. Briggs, L.M. Churgay, D.K. Clawson, et al., Crystal structure of the obese protein leptin-E100, Nature 387 (1997) 206–209.
[35] E. Haglund, J.I. Sulkowska, Z. He, G.S. Feng, P.A. Jennings, J.N. Onuchic, The unique cysteine knot regulates the pleotropic hormone leptin, PloS One 7 (2012), e45654.
[36] E. Haglund, J.I. Sulkowska, J.K. Noel, H. Lammert, J.N. Onuchic, P.A. Jennings, Pierced Lasso Bundles are a new class of knot-like motifs, PLoS Comput. Biol. 10 (2014), e1003613.
[37] E. Haglund, Engineering covalent loops in proteins can serve as an on/off switch to regulate threaded topologies, J. Phys. Condens. Matter 27 (2015) 354107.
[38] E. Haglund, A. Pilko, R. Wollman, P.A. Jennings, J.N. Onuchic, Pierced lasso topology controls function in leptin, J. Phys. Chem. B 121 (4) (2017) 706–718.
[39] P. Dabrowski-Tumanski, W. Niemyska, P. Pasznik, J.I. Sulkowska, LassoProt: server to analyze biopolymers with lassos, Nucleic Acids Res. 44 (2016) W383–W389.
[40] W. Niemyska, P. Dabrowski-Tumanski, M. Kadlof, E. Haglund, P. Sulkowski, J.I. Sulkowska, Complex lasso: new entangled motifs in proteins, Sci. Rep. 6 (2016) 36895.
[41] S.R. Presnell, F.E. Cohen, Topological distribution of four-alpha-helix bundles, Proc. Natl. Acad. Sci. U. S. A. 86 (1989) 6592–6596.
[42] B.R. Gibney, J.S. Johansson, F. Rabanal, J.J. Skalicky, A.J. Wand, P.L. Dutton, Global topology & stability and local structure & dynamics in a synthetic spin-labeled four-helix bundle protein, Biochemistry 36 (1997) 2798–2806.
[43] G. Bellesia, A.I. Jewett, J.E. Shea, Relative stability of de novo four-helix bundle proteins: insights from coarse grained molecular simulations, Protein Sci. 20 (2011) 818–826.
[44] A.D. Nagi, L. Regan, An inverse correlation between loop length and stability in a four-helix-bundle protein, Folding Des. 2 (1997) 67–75.
[45] W.D. Kohn, C.T. Mant, R.S. Hodges, Alpha-helical protein assembly motifs, J. Biol. Chem. 272 (1997) 2583–2586.
[46] M.J. Whitley, A.L. Lee, Frameworks for understanding long-range intra-protein communication, Curr. Protein Pept. Sci. 10 (2009) 116–127.
[47] J.W.J. Monod, J.P. Changeux, ON the nature OF allosteric transitions: a plausible model, J. Mol. Biol. 12 (1965) 88–118.
[48] J. Monod, F. Jacob, Teleonomic mechanisms in cellular metabolism, growth, and differentiation, Cold Spring Harbor Symp. Quant. Biol. 26 (1961) 389–401.
[49] G.M. Süel, S.W. Lockless, M.A. Wall, R. Ranganathan, Evolutionarily conserved networks of residues mediate allosteric communication in proteins, Nat. Struct. Biol. 10 (2003) 59–69.
[50] M. Kovermann, P. Rogne, M. Wolf-Watz, Protein dynamics and function from solution state NMR spectroscopy, Q. Rev. Biophys. 49 (2016) e6.
[51] M.P.M. Ricci, L. Narhi, T. Boone, D. Brems, Mutational approach to improve physical stability of protein therapeutics susceptible to aggregation. Role of altered conformation in irreversible precipitation, in: Misbehaving Proteins: Protein (Mis)folding, Aggregation, and Stability, Springer, New York, 2006.
[52] E. Haglund, J. Lind, T. Oman, A. Ohman, L. Mäler, M. Oliveberg, The HD-exchange motions of ribosomal protein S6 are insensitive to reversal of the protein-folding pathway, Proc. Natl. Acad. Sci. U. S. A. 106 (2009) 21619–21624.
[53] E. Haglund, J. Danielsson, S. Kadhirvel, M.O. Lindberg, D.T. Logan, M. Oliveberg, Trimming down a protein structure to its bare foldons: spatial organization of the cooperative unit, J. Biol. Chem. 287 (2012) 2731–2738.
[54] G. Lipari, A. Szabo, Model-free approach to the interpretation of nuclear magnetic resonance relaxation in macromolecules. 1. Theory and range of validity, J. Am. Chem. Soc. 104 (1982) 4546–4559.
[55] G. Lipari, A. Szabo, Model-free approach to the interpretation of nuclear magnetic resonance relaxation in macromolecules. 2. Analysis of experimental results, J. Am. Chem. Soc. 1 (1982) 4559–4570.
[56] M.W.G. Salzmann, K. Pervushin, H. Senn, K. Wüthrich, TROSY-type triple-resonance experiments for sequential NMR assignments of large proteins, J. Am. Chem. Soc. 121 (1999) 844–848.
[57] P. Schanda, H. Van Melckebeke, B. Brutscher, Speeding up three-dimensional protein NMR experiments to a few minutes, J. Am. Chem. Soc. 128 (2006) 9042–9043.
[58] J. Farjon, J. Boisbouvier, P. Schanda, A. Pardi, J.P. Simorre, B. Brutscher, Longitudinal-relaxation-enhanced NMR experiments for the study of nucleic acids in solution, J. Am. Chem. Soc. 131 (2009) 8571–8577.
[59] D. Frishman, P. Argos, Knowledge-based protein secondary structure assignment, Proteins 23 (1995) 566–579.
[60] E.G. Hutchinson, J.M. Thornton, PROMOTIF–a program to identify and analyze structural motifs in proteins, Protein Sci. 5 (1996) 212–220.
[61] J.A. Cuff, G.J. Barton, Evaluation and improvement of multiple sequence methods for protein secondary structure prediction, Proteins 34 (1999) 508–519.
[62] A. Figureau, M. Angélica Soto, J. Tohá, Secondary structure of proteins and three-dimensional pattern recognition, J. Theor. Biol. 201 (1999) 103–111.
[63] A. Figureau, M.A. Soto, J. Tohá, A pentapeptide-based method for protein secondary structure prediction, Protein Eng. 16 (2003) 103–107.
[64] J.A. Marsh, V.K. Singh, Z. Jia, J.D. Forman-Kay, Sensitivity of secondary structure propensities to sequence differences between alpha- and gamma-synuclein: implications for fibrillation, Protein Sci. 15 (2006) 2795–2804.
[65] D.H. Kim, K.H. Han, Transient secondary structures as general target-binding motifs in intrinsically disordered proteins, Int. J. Mol. Sci. 19 (2018).
[66] A. Sekhar, L.E. Kay, NMR paves the way for atomic level descriptions of sparsely populated, transiently formed biomolecular conformers, Proc. Natl. Acad. Sci. U. S. A. 110 (2013) 12867–12874.

[67] C. Lee, S.H. Park, M.Y. Lee, M.H. Yu, Regulation of protein function by native metastability, Proc. Natl. Acad. Sci. U. S. A. 97 (2000) 7727–7731.
[68] R.E. London, Chemical shift and linewidth characteristics of reversibly bound ligands, J. Magn. Reson., Ser. A 104 (1993) 190–196.
[69] J.L.E. Sudmeier, N.B.H. Jonsson, Dependence of NMR lineshape analysis upon chemical rates and mechanisms: implications for enzyme histidine titrations, J. Magn. Reson. 40 (1980) 377–390.
[70] T. Chouard, Structural biology: breaking the protein rules, Nature 471 (2011) 151–153.
[71] H. Lee, K.H. Mok, R. Muhandiram, K.H. Park, J.E. Suk, D.H. Kim, et al., Local structural elements in the mostly unstructured transcriptional activation domain of human p53, J. Biol. Chem. 275 (2000) 29426–29432.
[72] D.S. Wishart, B.D. Sykes, Chemical shifts as a tool for structure determination, Methods Enzymol. 239 (1994) 363–392.
[73] M.V. Berjanskii, D.S. Wishart, Application of the random coil index to studying protein flexibility, J. Biomol. NMR 40 (2008) 31–48.
[74] Y. Shen, A. Bax, Prediction of Xaa-Pro peptide bond conformation from sequence and chemical shifts, J. Biomol. NMR 46 (2010) 199–204.
[75] D. Fushman, O. Ohlenschlager, H. Ruterjans, Determination of the backbone mobility of ribonuclease T1 and its 2'GMP complex using molecular dynamics simulations and NMR relaxation data, J. Biomol. Struct. Dyn. 11 (1994) 1377–1402.
[76] P. Rossi, G.V. Swapna, Y.J. Huang, J.M. Aramini, C. Anklin, K. Conover, et al., A microscale protein NMR sample screening pipeline, J. Biomol. NMR 46 (2010) 11–22.
[77] H.P. Erickson, Size and shape of protein molecules at the nanometer level determined by sedimentation, gel filtration, and electron microscopy, Biol. Proced. Online 11 (2009) 32–51.
[78] J. Danielsson, J. Jarvet, P. Damberg, A. Graslund, Translational diffusion measured by PFG-NMR on full length and fragments of the Alzheimer A beta(1-40) peptide. Determination of hydrodynamic radii of random coil peptides of varying length, Magn. Reson. Chem. 40 (2002) S89–S97.
[79] I.R. Kleckner, M.P. Foster, An introduction to NMR-based approaches for measuring protein dynamics, Biochim. Biophys. Acta 1814 (2011) 942–968.
[80] J. Danielsson, M. Kurnik, L. Lang, M. Oliveberg, Cutting off functional loops from homodimeric enzyme superoxide dismutase 1 (SOD1) leaves monomeric β-barrels, J. Biol. Chem. 286 (2011) 33070–33083.
[81] L.E. Kay, D.A. Torchia, A. Bax, Backbone dynamics of proteins as studied by 15N inverse detected heteronuclear NMR spectroscopy: application to staphylococcal nuclease, Biochemistry 28 (1989) 8972–8979.
[82] N. Fernandez-Fuentes, J. Zhai, A. Fiser, ArchPRED: a template based loop structure prediction server, Nucleic Acids Res. 34 (2006) W173–W176.
[83] D. Tobi, I. Bahar, Structural changes involved in protein binding correlate with intrinsic motions of proteins in the unbound state, Proc. Natl. Acad. Sci. U. S. A. 102 (2005) 18908–18913.
[84] M. Arai, K. Sugase, H.J. Dyson, P.E. Wright, Conformational propensities of intrinsically disordered proteins influence the mechanism of binding and folding, Proc. Natl. Acad. Sci. U. S. A. 112 (2015) 9614–9619.
[85] P.J. Farber, A. Mittermaier, Relaxation dispersion NMR spectroscopy for the study of protein allostery, Biophys. Rev. 7 (2015) 191–200.
[86] S.W. Englander, N.R. Kallenbach, Hydrogen exchange and structural dynamics of proteins and nucleic acids, Q. Rev. Biophys. 16 (1983) 521–655.
[87] S.W. Englander, Protein folding intermediates and pathways studied by hydrogen exchange, Annu. Rev. Biophys. Biomol. Struct. 29 (2000) 213–238.
[88] A.R. Fersht, Structure and Mechanism in Protein Science: A Guide to Enzyme Catalysis and Protein Folding, W.H. Freeman and Co., New York, 1999.
[89] Z.Y. Kan, B.T. Walters, L. Mayne, S.W. Englander, Protein hydrogen exchange at residue resolution by proteolytic fragmentation mass spectrometry analysis, Proc. Natl. Acad. Sci. U. S. A. 110 (2013) 16438–16443.
[90] D.E. Otzen, O. Kristensen, M. Proctor, M. Oliveberg, Structural changes in the transition state of protein folding: alternative interpretations of curved chevron plots, Biochemistry 38 (1999) 6499–6511.
[91] Wang H, Logan DT, Danielsson J, Oliveberg M. Exposing the Distinctive Modular Behaviour of β-strands and α-helices in Folded Proteins. Unpublished results..
[92] H. Wang, L. Lang, D.T. Logan, J. Danielsson, M. Oliveberg, Tricking a protein to swap strands, J. Am. Chem. Soc. 138 (2016) 15571–15579.
[93] S. Grzesiek, A. Bax, Amino acid type determination in the sequential assignment procedure of uniformly 13C/15N-enriched proteins, J. Biomol. NMR 3 (1993) 185–204.
[94] S. Grzesiek, H. Dobeli, R. Gentz, G. Garotta, A.M. Labhardt, A. Bax, 1H, 13C, and 15N NMR backbone assignments and secondary structure of human interferon-gamma, Biochemistry 31 (1992) 8180–8190.
[95] L.E. Kay, G.Y. Xu, T. Yamazaki, Enhanced-sensitivity triple-resonance spectroscopy with minimal H2O saturation, J. Magn. Reson. 109 (1994) 129–133.
[96] M.J. Abraham, T. Murtola, R. Schulz, P. Szilárd, J.C. Smith, B. Hess, et al., GROMACS: high performance molecular simulations through multi-level parallelism from laptops to supercomputers, SoftwareX 1–2 (2015) 19–25.
[97] K. Lindorff-Larsen, S. Piana, K. Palmo, P. Maragakis, J.L. Klepeis, R.O. Dror, et al., Improved side-chain torsion potentials for the Amber ff99SB protein force field, Proteins 78 (2010) 1950–1958.